FLUID MECHANICS

Three-dimensional capillary ratchet-induced liquid directional steering

Shile Feng[1,2]†, Pingan Zhu[1]†, Huanxi Zheng[1], Haiyang Zhan[2], Chen Chen[2], Jiaqian Li[1], Liqiu Wang[3], Xi Yao[4], Yahua Liu[2], Zuankai Wang[1,5]*

Conventional understanding has it that a liquid deposited on a surface tends to move along directions that reduce surface energy, which is mainly dictated by surface properties rather than liquid properties, such as surface tension. Achieving well-controlled directional steering remains challenging because the liquid-solid interaction mainly occurs in the two-dimensional (2D) domain. We show that the spreading direction of liquids with different surface tensions can be tailored by designing 3D capillary ratchets that create an asymmetric and 3D spreading profile both in and out of the surface plane. Such directional steering is also accompanied by self-propulsion and high flow velocity, all of which are preferred in liquid transport.

Directional liquid transport is ubiquitous and critical to a range of practical applications, such as microfluidics (*1*), chemical reaction (*2*), water harvesting (*3*, *4*), and enhanced heat transfer (*5*). Recent efforts have demonstrated the feasibility of the spontaneous, rapid, and long-distance liquid transport on surfaces that are designed with gradients in topography (*6*–*8*), wettability (*9*, *10*), or surface charge density (*11*). In all of these studies, the liquid driving force is mainly determined by the gradients imposed by surfaces (*12*, *13*), and thus for a fixed design, the spreading direction of a liquid is not selectable by its intrinsic properties (*14*, *15*). For example, a liquid prefers to flow from the high-surface-energy area to the low-surface-energy area (*16*), as exemplified on wettability gradient surfaces that are driven by the unbalanced capillary force (*9*, *17*); from the high-curvature region to the low-curvature region on conical wires because of the difference in Laplace pressure (*18*); and from the higher liquid-pinning side to the less liquid-pinning side on asymmetric structures that result from the differentiated dynamics of liquid spreading (*12*).

We examined an unexpected liquid transport behavior on the *Araucaria* leaf, which consists of three-dimensional (3D) ratchets with transverse and longitudinal reentrant curvatures that are characterized by the low-surface-tension liquids selecting a pathway along the ratchet-tilting direction, whereas high-surface-tension liquids select an opposite

[1]Department of Mechanical Engineering, City University of Hong Kong, Hong Kong SAR 999077, P. R. China. [2]Key Laboratory for Precision and Non-traditional Machining Technology of Ministry of Education, Dalian University of Technology, Dalian 116024, P. R. China. [3]Department of Mechanical Engineering, The University of Hong Kong, Hong Kong SAR 999077, P. R. China. [4]Department of Biomedical Sciences, City University of Hong Kong, Hong Kong SAR 999077, P. R. China. [5]Center for Nature-Inspired Engineering, City University of Hong Kong, Hong Kong SAR 999077, P. R. China.
*Corresponding author. Email: zuanwang@cityu.edu.hk
†These authors contributed equally to this work.

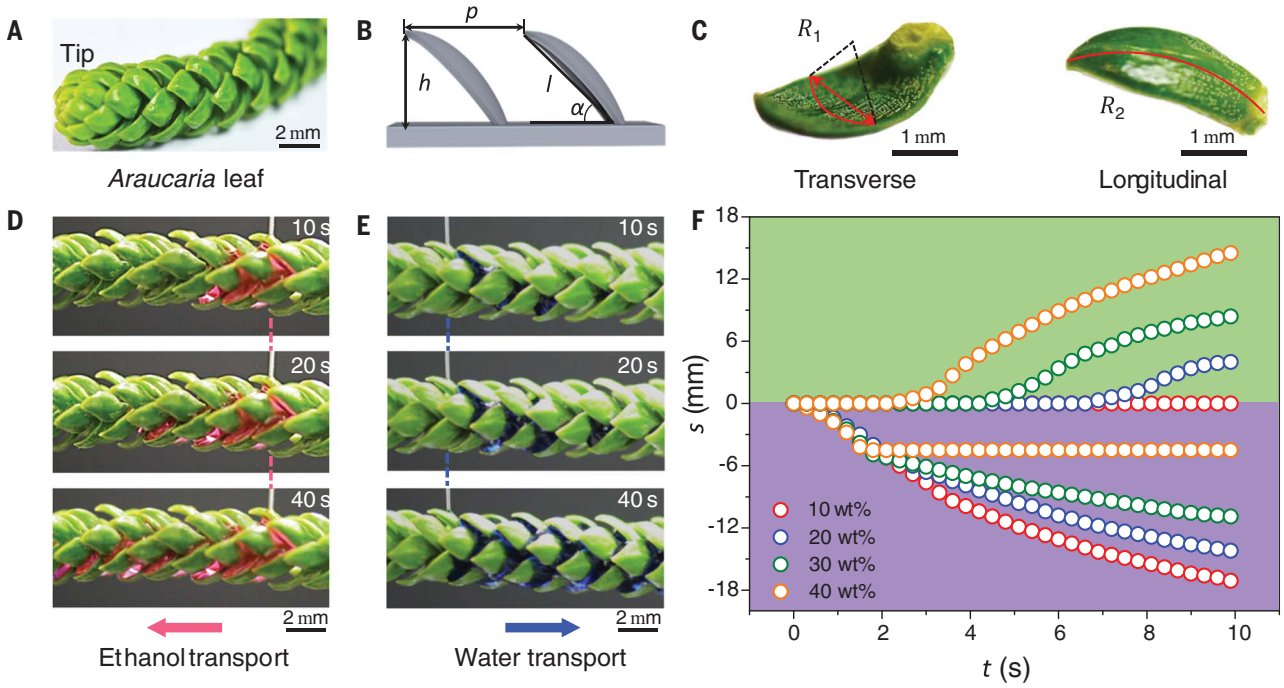

Fig. 1. Structural characteristics of *Araucaria* leaf for liquid directional steering. (**A**) Optical image of *Araucaria* leaf, which consists of periodically arranged ratchets tilting toward the leaf tip. (**B**) Structural characteristics of ratchet arrays. The height (h), tip-to-tip pitch (p), length (l), and tilt angle (α) of ratchets are ~2 mm, ~3 mm, ~2.6 mm, and ~40°, respectively. (**C**) Structural characteristics of a single ratchet. Each ratchet is endowed with the transverse curvature of radius R_1 and the longitudinal curvature of radius R_2. (**D** and **E**) Directional transport of ethanol and water on *Araucaria* leaf. Ethanol spreads along the ratchet-tilting direction (forward direction), whereas water spreads in the opposite direction (backward direction). (**F**) Transport distance (s) of water-ethanol mixtures with varied mass fraction (c) versus time (t) on *Araucaria* leaf. The transport distance s is positive for forward transport (green region) and negative for backward transport (purple region). For $c \leq 10\%$, the liquid only propagates in the backward direction with negative s; for $10 < c < 40\%$, the liquid transport is bidirectional; for $c \geq 40\%$, the liquid only propagates in the forward direction.

direction. Different from the conventional microstructures (*19*–*21*) that are widely used for directional liquid transport in the 2D domain (*22*–*26*), the *Araucaria* leaf and *Araucaria* leaf–inspired surface (ALIS) have 3D ratchets that enable liquid wicking both in and out of the surface plane. Moreover, the transverse and longitudinal reentrant curvatures impart asymmetric contact line pinning, which enables the directional steering and rapid transport of liquids with different surface tensions in a well-controlled manner.

The *Araucaria* leaf is found to consist of periodically arranged ratchets tilting toward the leaf tip (Fig. 1A). The height (h), pitch (p), length (l), and tilting angle (α) of ratchets are ~2 mm, ~3 mm, ~2.6 mm, and ~40°, respectively (Fig. 1B). Such ratchets exhibit dual-reentrant topography with a transverse curvature of radius R_1 and a longitudinal curvature of radius R_2 (Fig. 1C). The water and ethanol contact angles on the *Araucaria* leaf are ~59° and ~21°, respectively, suggesting a typical hydrophilic property (fig. S1). In contrast to our expectation, when continuously infusing water and ethanol (flow rate of 3 μl/s) on the *Araucaria* leaf, we found that ethanol spreads along the ratchet-tilting direction (Fig. 1D and movie S1A), whereas water propagates in an opposite direction (Fig. 1E and movie S1B). We define along the ratchet-tilting direction as the forward direction and against the ratchet-tilting direction as the backward direction.

We also investigated the liquid transport on the *Araucaria* leaf using water-ethanol mixtures that have different surface tensions (γ) and mass fractions of ethanol (c). Here, $c = m_e/(m_e + m_w)$, with m_e and m_w being the mass of ethanol and water, respectively. The correlation between γ and c is shown in fig. S2. When c ranges from 0 to 40%, γ decreases from 72 to 29 mN/m. The time-dependent variation of transport distance (s) is plotted in Fig. 1F for different water-ethanol mixtures. For $c \leq 10\%$, the liquid propagates only in the backward direction with negative s. For $10 < c < 40\%$, the liquid transport is bidirectional. For $c \geq 40\%$, the liquid propagates in the forward direction alone, although a slight backflow along the asymmetric ratchet was observed in the early stage of spreading (fig. S3).

Triggered by this observation, we implemented 3D printing to fabricate the ALIS. The ALIS consists of several parallel rows of ratchet arrays with pitch p = 750 μm, tilting angle α = 40°, height h = 800 μm, row-to-row width w = 1000 μm, interside-to-interside width d = 400 μm, R_1 = 400 μm, and R_2 = 650 μm (Fig. 2, A to C). We infused water-ethanol mixtures with c = 40% and c = 10% onto the ALIS at a flow rate of 3 μl/s, as shown in Fig. 2, D and E, respectively, and observed a similar transport behavior to that on the *Araucaria* leaf. The liquid mixture with c = 40% displays forward transport (Fig.

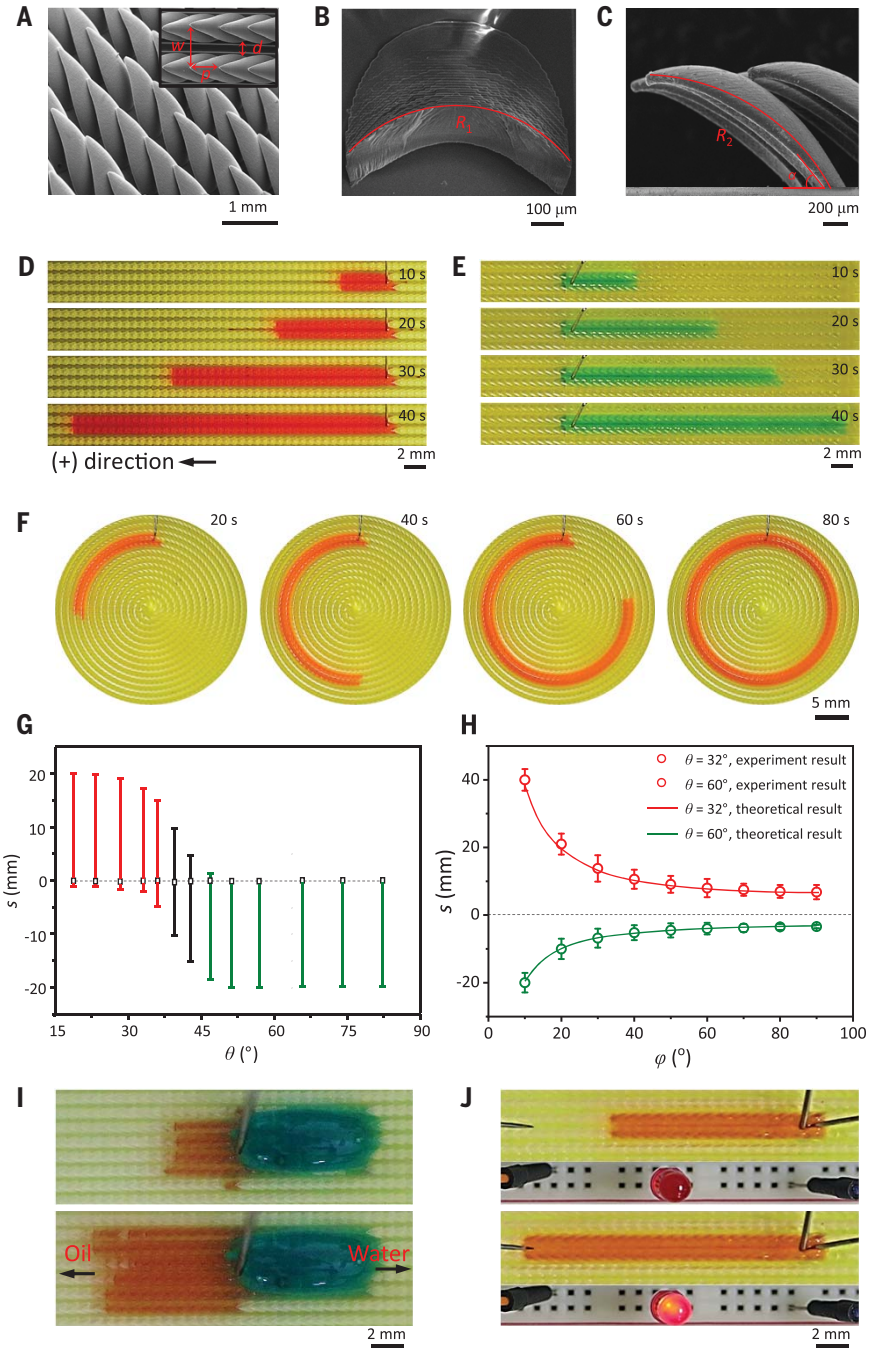

Fig. 2. Liquid directional steering on an ALIS. (**A** to **C**) Macro- and microstructures of ALIS. The row-to-row width w, interside-to-interside width d, and tip-to-tip pitch p are ~1000, 400, and 750 μm, respectively. The radii of transverse (R_1) and longitudinal (R_2) curvatures are ~400 and ~650 μm, respectively. The tilting angle of each ratchet is ~40°. (**D** and **E**) Transport of water-ethanol mixtures with c = 40% [red liquid (D)] and c = 10% [green liquid (E)] on ALIS. The liquid mixture with c = 40% displays forward transport, whereas that with c = 10% displays backward transport. (**F**) Directional spreading of liquid (θ = 32°) on circular ratchet arrays with a constant liquid width. (**G**) Variation in the transport distance s with contact angle θ, where s was measured after infusing the liquid for 60 s. As θ increases from ~20° to ~82°, the liquid transforms from forward transport to backward transport. (**H**) Plot of liquid transport on surfaces with different inclined angles φ (from 0° to 90°). The positive s stands for forward transport and negative s for backward transport. (**I**) Oil-water separation on ALIS. The liquid mixture contains water (dyed green) and oil (dyed red) with a volume ratio of 1:1. (**J**) Lighting up the light-emitting diode by directional transport of a conductive liquid on ALIS. The conductive liquid is a mixture of water, ethanol, and NaCl with a mass fraction of 40:9:1.

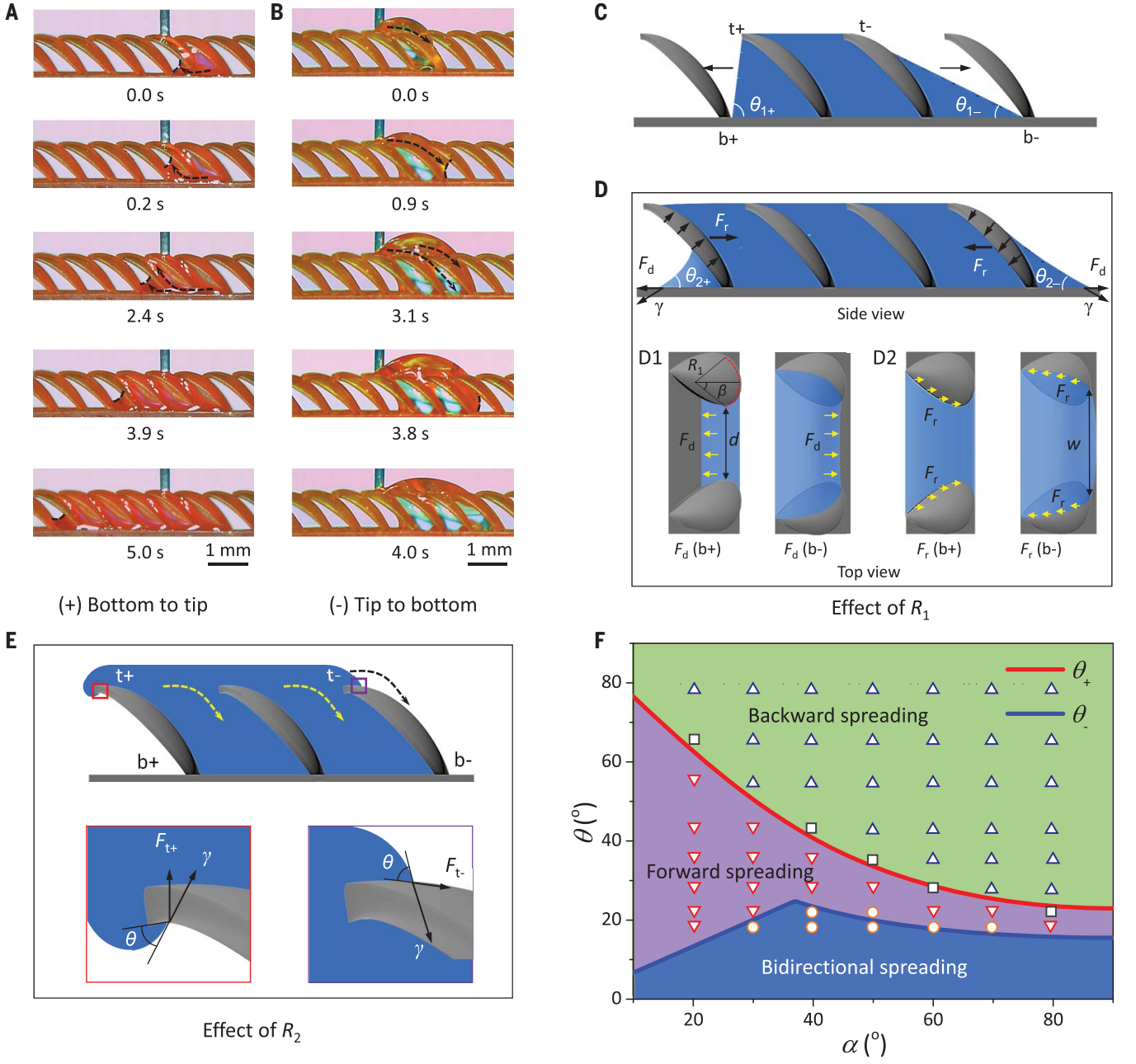

Fig. 3. Mechanism for liquid directional steering. (**A** and **B**) Two distinct spreading dynamics of liquids on ALIS. Liquid with θ = 32° wets the ratchet from bottom to top for forward spreading (A), whereas liquid with θ = 60° wets the ratchet from top to bottom for backward spreading (B). (**C**) Critical states for liquid spreading on ALIS. The symbols b+, b−, t+, and t− represent bottom-forward, bottom-backward, top-forward, and top-backward pinning sites, respectively. θ_{1+} and θ_{1-} are critical angles at which the liquid front reaches the b+ site and b− site, respectively. (**D**) Force analysis in the bottom-to-top wicking scenario with the transverse reentrant effect. The top-view schematics manifest the driving force at the bottom surface (D1) and the resistance force along the ratchets (D2) at the b+ site (left) and b− site (right), respectively. (**E**) Force analysis in the top-to-bottom wicking scenario with the longitudinal reentrant effect. In this scenario, the liquid is pinned at both the b+ and b− sites and subjected to asymmetric capillary forces at the t+ and t− sites. (**F**) Phase map for the directional steering of liquid transport. When $\theta_- < \theta < \theta_+$, liquid spreads forward (purple region marked with inverted triangle). When $\theta > \theta_+$, liquid spreads backward (green region marked with triangle). When θ is ~θ_+ (symbols marked with rectangle) or $\theta < \theta_- < \theta_+$ (blue region marked with circle), the liquid manifests a bidirectional transport.

2D and movie S2A), whereas the one with c = 10% displays backward transport (Fig. 2E and movie S2B). The width of the liquid barely changes during the spontaneous propagation on straight (Fig. 2, D and E) and circular (Fig. 2F and movie S3) ratchet arrays. These results are distinct from previous studies in which the liquid puddle gradually widens during spreading (*12*), which indicates the strong pinning of the liquid front by the curved shape of 3D ratchets (Fig. 2, B and C). Essentially, the ALIS can be treated as 3D capillary ratchets (*22*), whose characteristic lengths are comparable with the capillary length $l_c = (\gamma/\rho g)^{1/2}$. Here, γ, ρ, and g are the liquid surface tension, liquid density, and gravitational acceleration, respectively.

The transport distance s of liquids with different surface tensions γ on the ALIS is plotted in Fig. 2G, where s was measured after infusing liquids for 60 s. The liquid contact angles increase with the surface tension of liquids

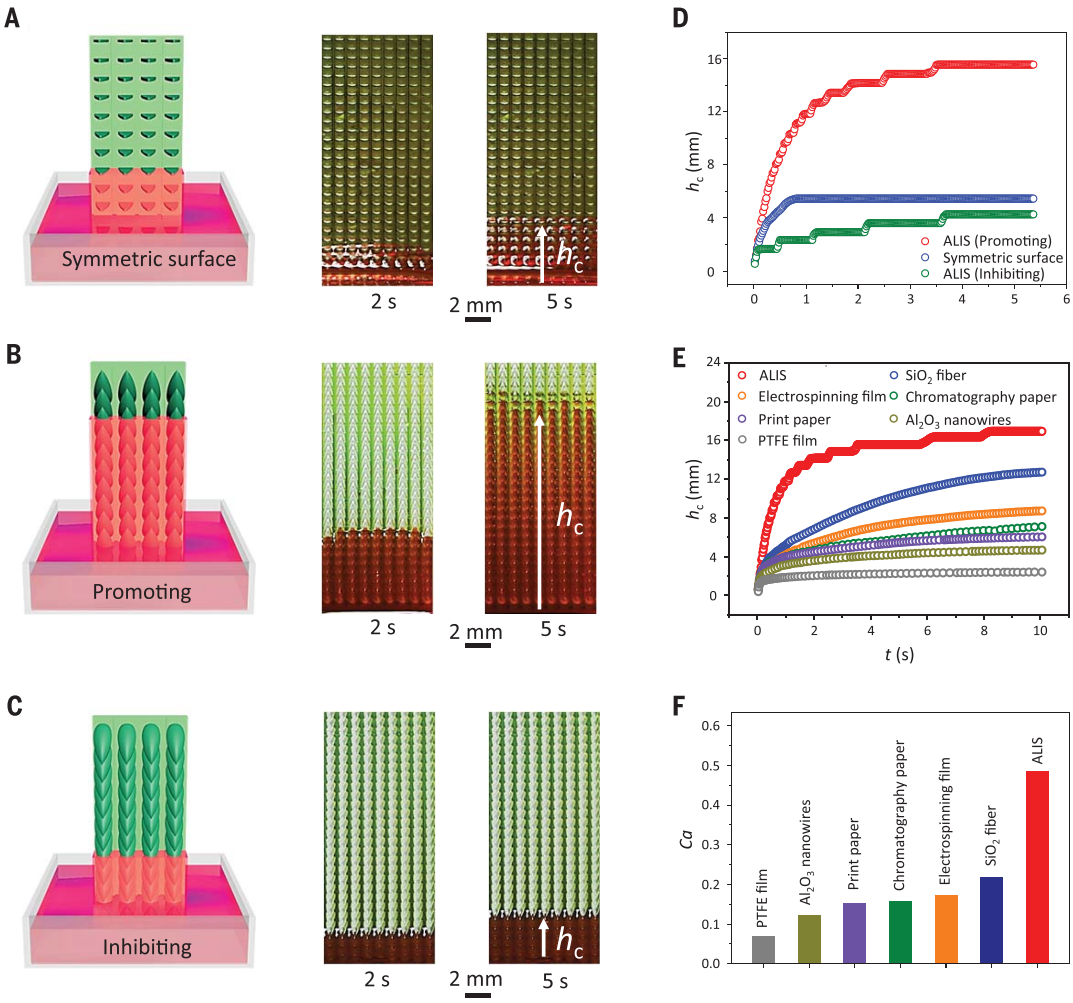

Fig. 4. Promoting or inhibiting capillary rise by the ALIS. (**A**) Capillary rise of liquid on a symmetric surface. The height of capillary rise h_c reaches ~6 mm in 5 s. (**B**) Promoting capillary rise on ALIS when the ratchet is tilting upward. h_c reaches ~16 mm in 5 s. (**C**) Inhibiting capillary rise on ALIS with ratchet tilting downward. h_c is only ~4 mm in 5 s. (**D**) Variation of capillary rise height h_c as a function of time t on ALIS and symmetric surface. (**E** and **F**) Height h_c (E) and capillary number Ca (F) on various surfaces, including polytetrafluoroethylene (PTFE) membrane, print paper, SiO_2 fibers, Al_2O_3 nanowires, electrospinning film, chromatography paper, and ALIS. $Ca = V\eta/\gamma$, representing the dimensionless velocity in which the average wicking velocity V (measured in the first 1.5 s) is normalized by the characteristic capillary velocity γ/η, denoting γ and η as the surface tension and viscosity of liquids, respectively. Both the height and velocity on the ALIS (in promoting mode) are much larger than those on other surfaces during the same transport period.

on a flat surface with the same material as that of the ALIS (fig. S4). We found that as the equilibrium contact angle (θ) increases from ~20° to ~82°, the transport direction is reversed from forward to backward, during which the crossover occurs at θ = 42° ± 5°, featuring a bidirectional mode (Fig. 2G and figs. S5 and S6). These observations suggest that the spreading direction of liquids on a predetermined ALIS can be selected, with high-surface-tension liquids preferring the backward direction, whereas low-surface-tension liquids select the forward direction. Such directional steering is still maintained when the ALIS is placed under a tilt angle φ (0° < φ ≤ 90°), although the transport distance s becomes reduced with an increase in φ (Fig. 2H). The measured s shows good agreement with the theoretical data predicted by $s = [(\cos\theta - \cos\theta_c)\gamma]/(\rho g h \cos\theta_c \sin\varphi)$, for which we denote θ_c, ρ, and g as the critical contact angle for capillary wicking (*27*), liquid density, and gravitational acceleration, respectively (fig. S7). The liquid spreading is almost self-propelled at a low liquid-flow rate (~3 μl/s), above which the inertia effect starts to become non-negligible (fig. S8).

The well-controlled selection of liquid spreading direction can be harnessed for immiscible water-oil (such as dichloroethane) separation. When infusing a water-oil mixture on the ALIS with a volume ratio of 1:1, the oil and water display opposite transport directions, and a complete separation is achieved without the need of gravity (Fig. 2I), as opposed to existing separation strategies. In addition, the unidirectional transport of water on the ALIS can be used to switch on the originally isolated circuit and light up a light-emitting diode, which provides a simple route to construct a fluidic gate (Fig. 2J).

To explain the mechanisms responsible for the liquid directional steering, we first examined contact lines of two representative liquids with θ = 32° and θ = 60°. Initially, when being filled in an asperity between two adjacent ratchets (Fig. 3, A and B), liquids are confined by four critical sites (fig. S9) at the bottom forward (b+), bottom backward (b–), top forward (t+), and top backward (t–). Liquid with θ = 32° first breaks the pinning at the b+ site and then wets the ratchet from bottom to top. As it rises, a new cycle of bottom-to-top rising occurs, leading to a continuous, long-range propagation in the forward direction (Fig. 3A, fig. S10A, and movie S4A). By contrast, the liquid with θ = 60° is pinned at both the b+ and b– sites, selects the pathway toward the top (t+ and t–) sites, and propagates along the backward direction through a continuous top-to-bottom wicking (Fig. 3B, fig. S10B, and movie S4B).

We then resorted to a force analysis (*28*, *29*) to probe how a liquid selects its spreading direction (Fig. 3, C to E). For the bottom-to-top rising scenario (Fig. 3A), the spontaneous transport in a preferential direction requires two conditions. First, the liquid should be able to reach the next ratchet, which requires a smaller-equilibrium liquid contact angle compared with two critical angles defined by surface geometry, θ_{1+} and θ_{1-} (Fig. 3C), which are expressed as $\theta_{1+} = \arctan[l\sin\alpha/(p - l\cos\alpha)]$ and $\theta_{1-} = \arctan[l\sin\alpha/(p + l\cos\alpha)]$, respectively (fig. S11). Second, driving forces on the liquid front should be large enough to overcome the pinning effect. For an ALIS, the distinct structures generate a driving force (F_d) at the contact line at the bottom surface (Fig. 3D, side and top view of D1), as well as a resistance force (F_r) at the contact line along the

ratchets (Fig. 3D, side and top view of D2). Briefly, at the b+ site, F_d scales as ~$d\gamma\cos\theta$ and F_r ~$2l\gamma\sin\alpha\sin(\theta + \beta)$, where β is the semiangle for the transverse ratchet arc (Fig. 3D). Balancing F_d with F_r, we have a critical angle $\theta_{2+} = \arccos[2l\sin\alpha\sin(\theta_{2+} + \beta)/d]$. Similarly, at the b− site, another critical angle, $\theta_{2-} = \arctan[w/(2l\sin\alpha)]$, is derived by balancing $F_d = w\gamma\cos\theta$ and $F_r = 2l\gamma\sin\alpha\sin\theta$ (figs. S12 and S13). The presence of a transverse reentrant curvature creates an apparent difference in θ_{2+} and θ_{2-} on one surface (Fig. 3D), opening up the room for liquids to exhibit an asymmetric spreading and to select direction along the surface.

By combining the above force analysis, the forward transport through a continuous, bottom-to-top rising demands that the equilibrium liquid contact angle falls between $\theta_- < \theta < \theta_+$ (Fig. 3F), where $\theta_+ = \min[\theta_{1+}, \theta_{2+}]$ and $\theta_- = \min[\theta_{1-}, \theta_{2-}]$ (fig. S14). Taking $\alpha = 40°$, for example, θ_+ and θ_- predicted by our model are 42° and 23°, respectively. When $23° < \theta < 42°$, we expect a forward spreading, which was indeed observed in our experiments (Fig. 3F).

Although the above force analysis can successfully explain the pinning at the bottom surface (in plane) and predict the spreading direction, it is incapable of explaining the pinning effect at the top of the 3D surface (out of the plane). For $\theta > \theta_+$, an asymmetric pinning and subsequent backward spreading through a top-to-bottom wicking were observed in Fig. 3B. To elucidate this unexpected phenomenon, we further considered the reentrant effect of longitudinal curvature. The reentrant structure at the t+ site produces an upward capillary force normal to the ratchet surface, written as $F_{t+} = \gamma\sin\theta$, that pins the liquid at the asperity of the ALIS (Fig. 3E, schematic in red rectangle). However, such a pinning effect is absent at the t− site, where a driving force along the surface ($F_{t-} = \gamma\cos\theta$) is present (Fig. 3E, schematic in purple rectangle). Under such a force asymmetry imposed by the longitudinal reentrant effect, a backward flow is favorably selected for liquid with $\theta > \theta_+ = 42°$ for the ALIS with $\alpha = 40°$.

The cooperation between the transverse and longitudinal reentrant curvature imparts an asymmetric force pinning in a 3D profile. By contrast, control surfaces without the presence of 3D capillary ratchets, including 1D stripes (fig. S15A) and 2D ratchets (fig. S15B), are only associated with contact line pinning in the plane. Thus, liquids of different surface tensions can only manifest a unidirectional transport in one way or bidirectional spreading (fig. S15 and movies S5 and S6), which eliminates the possibility for direction selection. Otherwise, a dynamic top-to-bottom wicking on the surface and subsequent spreading will not occur (*21*).

To fully build the phase map for the liquid spreading, we also considered the bidirectional transport that occurs in the transitioning region when $\theta \approx \theta_+$ (Fig. 3F, rectangles) or $\theta < \theta_- < \theta_+$ (Fig. 3F, blue region, circles). In particular, in the first case, the bidirectional transport is characterized by the manifestation of both bottom-to-top rising (forward mode) and top-to-bottom wicking (backward mode), as evidenced in our experimental visualization (fig. S6 and movie S7).

The liquid directional steering can be mutually used to promote liquid transportation such as in textile dying (*30*), inkjet printing (*31*, *32*), and seawater desalination (*33*) or to inhibit liquid wicking such as in anticorrosion and microbial spreading. To demonstrate this, we first investigated liquid transport on a surface with symmetric ratchets ($\alpha = 90°$). When the surface is inserted into a bath of ethanol, a capillary rise with a height (h_c) of ~6 mm is achieved within 5 s (Fig. 4A and movie S8). By contrast, the capillary rise on the ALIS is ~16 mm (Fig. 4B and movie S9), suggesting a notable enhancement in the spreading. However, the capillary rise can also be inhibited by designing an ALIS with the ratchet structures arranged downward (Fig. 4C and movie S10), which can be used in certain conditions in which a minimal liquid propagation is preferred. The role of the 3D capillary ratchets in promoting or inhibiting liquid wicking (Fig. 4D) is further illustrated by comparing capillary rise heights (Fig. 4E and fig. S16) on different samples, including polytetrafluoroethylene membrane, print paper, silicon dioxide (SiO_2) fibers, aluminium oxide (Al_2O_3) nanowires, electrospinning film, and chromatography paper. At the beginning of capillary rise, the measured height is consistent with that predicted by the Washburn law, which follows $h_c \sim[2\gamma h(\cos\theta - \cos\theta_c)t/3\eta\cos\theta_c]^{1/2}$ (*27*, *34*). Later, gravity becomes important, and h_c diverges on different surfaces (fig. S16). In Fig. 4F, we compare the wicking velocities on different samples, which demonstrates the intriguing prospect of the ALIS in achieving rapid liquid transport without the need for nanoscale structures. Taken together, our work demonstrates that the 3D capillary ratchets can be cleverly harnessed to impart many advantages for fluid flow, such as well-controlled directional steering, self-propulsion, high velocity, and long-distance transport.

REFERENCES AND NOTES

1. R. Seemann, M. Brinkmann, T. Pfohl, S. Herminghaus, *Rep. Prog. Phys.* **75**, 016601 (2012).
2. H. A. Stone, A. D. Stroock, A. Ajdari, *Annu. Rev. Fluid Mech.* **36**, 381–411 (2004).
3. Y. Zheng *et al*., *Nature* **463**, 640–643 (2010).
4. K. C. Park *et al*., *Nature* **531**, 78–82 (2016).
5. J. Li *et al*., *Nat. Phys.* **12**, 606–612 (2016).
6. K. H. Chu, R. Xiao, E. N. Wang, *Nat. Mater.* **9**, 413–417 (2010).
7. Q. Wang, X. Yao, H. Liu, D. Quéré, L. Jiang, *Proc. Natl. Acad. Sci. U.S.A.* **112**, 9247–9252 (2015).
8. H. Chen *et al*., *Nature* **532**, 85–89 (2016).
9. M. K. Chaudhury, G. M. Whitesides, *Science* **256**, 1539–1541 (1992).
10. N. A. Malvadkar, M. J. Hancock, K. Sekeroglu, W. J. Dressick, M. C. Demirel, *Nat. Mater.* **9**, 1023–1028 (2010).
11. Q. Sun *et al*., *Nat. Mater.* **18**, 936–941 (2019).
12. J. Li *et al*., *Sci. Adv.* **3**, eaao3530 (2017).
13. C. Li *et al*., *Proc. Natl. Acad. Sci. U.S.A.* **116**, 12704–12709 (2019).
14. P. Comanns *et al*., *J. R. Soc. Interface* **12**, 20150415 (2015).
15. Y. Liu *et al*., *Small* **16**, e1901819 (2020).
16. J. C. Bird, S. Mandre, H. A. Stone, *Phys. Rev. Lett.* **100**, 234501 (2008).
17. S. Daniel, M. K. Chaudhury, J. C. Chen, *Science* **291**, 633–636 (2001).
18. C. Lv *et al*., *Phys. Rev. Lett.* **113**, 026101 (2014).
19. A. Tuteja *et al*., *Science* **318**, 1618–1622 (2007).
20. T. L. Liu, C.-J. C. Kim, *Science* **346**, 1096–1100 (2014).
21. W. Choi, A. Tuteja, J. M. Mabry, R. E. Cohen, G. H. McKinley, *J. Colloid Interface Sci.* **339**, 208–216 (2009).
22. M. Prakash, D. Quéré, J. W. Bush, *Science* **320**, 931–934 (2008).
23. C. Liu, J. Ju, Y. Zheng, L. Jiang, *ACS Nano* **8**, 1321–1329 (2014).
24. J. Li *et al*., *Small* **16**, e1901751 (2020).
25. S. Feng *et al*., *Sci. Adv.* **6**, eabb4540 (2020).
26. H. Linke *et al*., *Phys. Rev. Lett.* **96**, 154502 (2006).
27. J. Bico, C. Tordeux, D. Quéré, *Europhys. Lett.* **55**, 214–220 (2001).
28. P. A. Zhu *et al*., *Mater. Horiz.* **5**, 1156–1165 (2018).
29. X. Tian, V. Jokinen, J. Li, J. Sainio, R. H. A. Ras, *Adv. Mater.* **28**, 10652–10658 (2016).
30. M. T. Tyree, *Nature* **423**, 923–923 (2003).
31. S. Zheng *et al*., *Adv. Funct. Mater.* **28**, 1800832 (2018).
32. J. Z. Wang, Z. H. Zheng, H. W. Li, W. T. Huck, H. Sirringhaus, *Nat. Mater.* **3**, 171–176 (2004).
33. L. Wu *et al*., *Nat. Commun.* **11**, 521 (2020).
34. E. W. Washburn, *Phys. Rev.* **17**, 273–283 (1921).

ACKNOWLEDGMENTS

Funding: We acknowledge financial support from the Research Grants Council of Hong Kong (C1006-20WF, 11213320, and 17205421), Shenzhen Science and Technology Innovation Council (JCYJ20170413141208098), Innovation Technology Fund (GHP/021/19SZ), Tencent Foundation through the XPLORER PRIZE, National Natural Science Foundation of China (52005075), Fundamental Research Funds for the Central Universities [DUT19RC(3)055], and Star Ocean Outstanding Talents Program. **Author contributions:** S.F. and Z.W. conceived the research. Z.W. supervised the research. S.F. carried out the experiment. Hu.Z. and Ha.Z. prepared the samples, and C.C. and Y.L. designed the experimental apparatus. S.F., P.Z., and J.L. developed the theoretical model. L.W. and X.Y. examined and polished the manuscript. All authors analyzed data and wrote the paper. **Competing interests:** The authors declare no competing financial interests. **Data and materials availability:** All data are available in the main text or the supplementary materials.

SUPPLEMENTARY MATERIALS

Materials and Methods
Figs. S1 to S16
Movies S1 to S10

26 January 2021; accepted 13 August 2021
10.1126/science.abg7552

Science

Three-dimensional capillary ratchet-induced liquid directional steering

Shile FengPingan ZhuHuanxi ZhengHaiyang ZhanChen ChenJiaqian LiLiqiu WangXi YaoYahua LiuZuankai Wang

Science, 373 (6561), • DOI: 10.1126/science.abg7552

Surfaces directing fluid flows

Although surfaces can be made to attract or repel liquids using coatings, surface textures with specific curvature can also be used to achieve the same effect. However, fluid transport is usually limited by the specific pattern that only drives flow at the surface itself. Feng *et al*. created a dual-reentrant surface that has an asymmetric profile so that fluids spread out at the surface and subsurface layers. Furthermore, these surfaces can be designed so that different liquids will naturally steer in opposing directions simply because of their specific interactions with the surface. —MSL